

# Modeling of Cosmic-Ray Production and Transport and Estimation of Gamma-Ray and Neutrino Emissions in Starburst Galaxies

Ji-Hoon Ha,<sup>1</sup> Dongsu Ryu,<sup>1</sup> AND Hyesung Kang<sup>2</sup>

<sup>1</sup>*Department of Physics, School of Natural Sciences, UNIST, Ulsan 44919, Korea*

<sup>2</sup>*Department of Earth Sciences, Pusan National University, Busan 46241, Korea*

(Received; Revised; Accepted)

Submitted to The Astrophysical Journal

## ABSTRACT

Starburst galaxies (SBGs) with copious massive stars and supernova (SN) explosions are thought to be sites of active cosmic-ray (CR) production. Based on detailed predictions of the nonlinear diffusive shock acceleration (DSA) theory, we calculate the cosmic-ray proton (CRP) production due to both pre-SN stellar winds (SWs) and supernova remnants (SNRs) from core-collapse SNe inside the starburst nucleus (SBN). Adopting different models of the CRP transport in the SBN, we estimate the emissions of  $\gamma$ -rays and neutrinos due to inelastic  $pp$  collisions from nearby SBGs such as M82, NGC253, and Arp220. We find that the  $\gamma$ -rays observations by Fermi-LAT, Veritas, and H.E.S.S. can be reproduced reasonably well with different models for the CRP production and transport, but the best results are obtained with the combination of the double power-law model for the SNR-produced CRP distribution, and the diffusion model where the scattering of CRPs is controlled mostly by the self-excited turbulence due to CRP streaming instability. The contribution of SW-produced CRPs may depend on the integrated galactic initial mass function, and could be substantial in Arp220 where the star formation rate is high. We confirm that the neutrino fluxes from nearby SBGs are too small to be detected as point sources in IceCube. On the other hand, M82 and NGC253 might be detectable as point sources in the upcoming KM3NeT, but only when the most optimistic models are employed.

*Keywords:* cosmic rays – galaxies: starburst – gamma rays – neutrinos

## 1. INTRODUCTION

A starburst galaxy (SBG) is characterized by a nuclear region, named as starburst nucleus (SBN), with enhanced star formation rate (SFR) (e.g., Kennicutt & Evans 2012, and references therein). Young massive stars blow powerful stellar winds (SWs) throughout their lifetime and die in spectacular explosions as core-collapse supernovae (SNe) (Weaver et al. 1977; Freyer et al. 2003; Georgy et al. 2013; Janka 2012). Various shock waves driven by these activities can accelerate cosmic-rays (CRs) primarily through diffusive shock acceleration (DSA) (e.g., Drury 1983). Some of mechanical energy of SWs is expected to be converted to CRs at termination shocks in stellar wind bubbles and super-

bubbles created by young star clusters, colliding-wind shocks in binaries of massive stars, and bow shocks of massive runaway stars (e.g., Casse & Paul 1980; Cesarsky & Montmerle 1983; Bykov 2014). Seo et al. (2018), for instance, estimated that the energy deposited by SWs could reach up to  $\sim 25\%$  of that from SNe in our Galaxy. In SBGs, the relative contribution of SWs could be more important, since the integrated galactic initial mass function (IGIMF) is in general flatter for higher SFR (e.g., Palla et al. 2020). Supernova remnant (SNR) shocks driven by core-collapse SNe propagate into the pre-SN winds with  $\rho \propto r^{-2}$  density profile and strong magnetic fields, so the blast waves do not decelerate significantly and the maximum energy of CR nuclei accelerated by such shocks could reach up to  $\sim 100$  PeV (e.g., Berezhko & Völk 2000; Zirakashvili & Ptuskin 2018). Hence, the SBNs of SBGs have been recognized as sites of very active CR production (e.g., Peretti et al. 2019; Bykov et al. 2020).

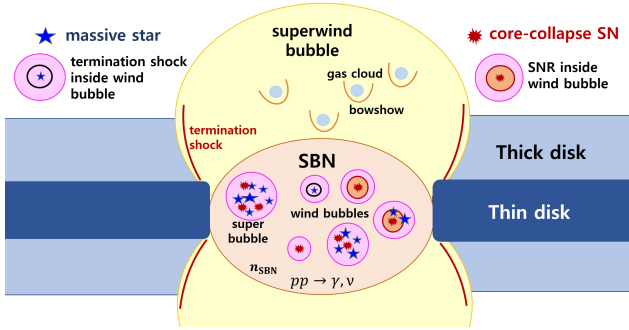


**Figure 1.** Schematic diagram illustrating a variety of shocks in the central region of SBGs: (1) termination shocks inside stellar wind bubbles or superbubbles created by star clusters (Freyer et al. 2003), (2) blast waves from core-collapse SNe inside stellar wind bubbles or superbubbles (Berezhko & Völk 2000), (3) the termination shock of superwind bubble created by the supersonic outflow from the SBN (Romero et al. 2018), (4) bow shocks around gas clouds colliding with the superwind from the SBN (Müller et al. 2020). This study focuses on the CRP production inside the SBN and the ensuing  $\gamma$ -ray and neutrino emissions due to inelastic  $pp$ -collisions.

In addition, the collective input of massive SWs and SN explosions can induce supersonic outflows in SBGs, known as SBN winds, and create superwind bubbles around the SBN. It has been proposed that the termination shocks of the superwind and bow shocks formed around gas clouds embedded in the outflows can provide additional sources of the CR acceleration (Romero et al. 2018; Müller et al. 2020). In this study, we focus on the CR acceleration at shocks induced by SWs and SNRs inside the SBN (see Figure 1).

The beauty of the original DSA predictions lies in the simple power-law (PL) momentum distribution,  $f_p(p) \propto p^{-q}$ , in the test-particle regime, where the PL slope,  $q = 4M_s^2/(M_s^2 - 1)$ , depends only on the shock sonic Mach number,  $M_s$  (e.g., Drury 1983, and see further discussions in Section 2.1). According to the nonlinear theory of DSA, however, with a conversion efficiency of order of 10 % from the shock kinetic energy to the CR energy at strong shocks, the dynamical feedback of CR protons (CRPs) leads to a substantial concave curvature in their momentum distribution (e.g., Berezhko & Ellison 1999; Caprioli et al. 2009; Kang 2012; Bykov et al. 2014). However, the time-integrated, cumulative CRP spectra produced during the SNR evolution seem to exhibit much smaller concavities, compared to the instantaneous spectra at the shock position at a given age (e.g., Caprioli et al. 2010; Zirakashvili & Ptuskin 2012; Kang 2013). The important caveat here is that the physics of DSA has yet to be fully understood from the

first principles in order to make quantitative predictions (e.g. Marcowith et al. 2016). In this study, in addition to the canonical single PL form, we adopt double PL momentum spectra to represent the concave spectra of CRPs that might be produced by an ensemble of SNRs with wide ranges of parameters at different dynamical stages.

CRPs in the SBN can inelastically collide with background thermal protons ( $pp$  collisions) and produce neutral and charged pions, which decay into  $\gamma$ -rays and neutrinos, respectively. Indeed,  $\gamma$ -rays from SBGs have been observed using Fermi-LAT (e.g., Abdo et al. 2010; Acero et al. 2015; Peng et al. 2016; Abdollahi et al. 2020) and ground facilities, such as H.E.S.S. and Veritas (e.g., VERITAS Collaboration et al. 2009; Acero et al. 2009; The VERITAS Collaboration et al. 2015; H. E. S. S. Collaboration et al. 2018), proving the active acceleration of CRPs in SBGs. Although SBGs have not yet been identified as point sources of neutrinos, they have been considered to be potential contributors of high energy neutrinos observable in IceCube (e.g., Loeb & Waxman 2006; Murase et al. 2013; Tamborra et al. 2014; Bechtol et al. 2017). Tamborra et al. (2014), for instance, adopting a scaling relation between  $\gamma$ -ray and infrared luminosities, estimated the  $\gamma$ -ray background and the diffuse high-energy neutrino flux from star-forming galaxies (SFGs) including SBGs, and suggested that SBGs could be the main sources of IceCube neutrinos. Bechtol et al. (2017), on the other hand, argued that considering the contribution from blazars, SFGs may not be the primary sources of IceCube neutrinos. In addition, Peretti et al. (2020) argued that SBGs would be hard to be detected as point neutrino sources in IceCube.

There have been previous studies to explain the observed spectra of SBGs in  $\gamma$ -rays (as well as in other frequency ranges) and to predict neutrino emissions (e.g., Wang & Fields 2018; Sudoh et al. 2018; Peretti et al. 2019, 2020; Krumholz et al. 2020, for recent works). The hadronic process for the production of  $\gamma$ -rays and neutrinos is governed mainly by the “production” and “transport” of CRPs. In most of these studies, the CRPs are assumed to be produced at SNR shocks, and the cumulative momentum distribution of CRPs inside the SBN is described with a single PL spectrum ( $\propto p^{-\alpha}$ ); the Fermi-LAT  $\gamma$ -ray observations for well-studied SBGs, such as M82, NGC253, and Arp220, require the CRP momentum distribution with  $\alpha \sim 4.2 - 4.5$ .

The transport of CRPs in the SBN is expected to be regulated by the advection due to the superwinds escaping from the SBN and the diffusion mediated by magnetic turbulence. The wind transport is energy-independent and the advection time scale of CRPs would

be comparable to the energy loss time scale in SBGs (e.g., Peretti et al. 2019). On the contrary, the transport due to diffusion is expected to depend on the CRP energy. The diffusion has been modeled, for instance, with the large-scale, Kolmogorov-type turbulence of  $\delta B/B \sim 1$  expected to be present in the interstellar medium (ISM) (e.g., Sudoh et al. 2018; Peretti et al. 2019), and then for most CRPs, the diffusion time scale is longer than the energy loss time scale. Krumholz et al. (2020), on the other hand, argued that the turbulence of scales less than the gyroradius of CRPs with  $E_{\text{CR}} \lesssim \text{several} \times 0.1 \text{ PeV}$  would be wiped out by ion-neutral damping, and suggested that CRPs interact mostly with the Alfvén waves that are self-excited via CRP streaming instability. With this model, the diffusion time scale is much shorter, and in the energy range of  $E_{\text{CR}} \gtrsim 1 \text{ TeV}$ , CRPs are inefficiently confined in the SBN.

Previous studies have been successful to some degree in reproducing  $\gamma$ -ray observations. In this work, we expand such efforts to provide an improved theoretical model of the CRP production in the SBN and the estimation of  $\gamma$ -ray and neutrino emissions for nearby SBGs, specifically, M82, NGC253, and Arp220. Firstly, in addition to single PL momentum distributions, we consider double PL distributions for SNR-produced CRPs. This is partly motivated by the employment of double PLs in fitting observed  $\gamma$ -ray spectra (e.g., Tamborra et al. 2014; Bechtol et al. 2017), but also by theoretical consideration for the DSA theory as discussed above. Secondly, we adopt different diffusion models for the diffusive transport of CRPs in the SBN, specifically the model where CRPs scatter off large-scale, Kolmogorov turbulence, and the model suggested by Krumholz et al. (2020). We will examine the consequence of different momentum distributions combined with different diffusion models for the emissions of  $\gamma$ -ray and neutrinos from SBGs.

This paper is organized as follows. In Sections 2 and 3, we detail models for the production and transport of CRPs in the SBN. In Sections 4 and 5, we present the estimates of  $\gamma$ -rays and neutrinos from SBGs. A summary follows in Section 6.

## 2. COSMIC-RAY PRODUCTION IN SBN

### 2.1. Physics of Nonlinear DSA

In general, the physics of DSA is governed mainly by both the sonic and Alfvén Mach numbers and the obliquity angle of magnetic fields in the background flow (e.g., Balogh & Treumann 2013; Marcowith et al. 2016). The outcomes of DSA, in fact, depend on nonlinear interrelationships among complex kinetic processes, including

**Table 1.** Parameters of Three Nearby SBGs Used in Modelings

	M82	NGC253	Arp220
$z^a$	$9 \times 10^{-4}$	$8.8 \times 10^{-4}$	$1.76 \times 10^{-2}$
$D_L \text{ [Mpc]}^a$	3.9	3.8	77
$R_{\text{SBN}} \text{ [pc]}^a$	220	150	250
$n_{\text{SBN}} \text{ [cm}^{-3}]^a$	175	250	3500
$\mathcal{R}_{\text{SN}} \text{ [yr}^{-1}]^a$	0.05	0.027	2.25
$v_{\text{SBNwind}} \text{ [km s}^{-1}]^a$	600	300	500
$H_{\text{gas}} \text{ [pc]}^b$	73	130	75
$M_{\text{A,turb}}^b$	2	2	2
$v_{\text{Ai}} \text{ [km s}^{-1}]^b$	880	920	$3,500/\sqrt{10}$
$\mathcal{L}_{\text{SN}} \text{ [10}^{40} \text{ erg s}^{-1}]^c$	159	85.6	7140
$\mathcal{L}_{\text{SW}} \text{ [10}^{40} \text{ erg s}^{-1}]^c$	49	26.2	6200

<sup>a</sup>  $z$  and  $D_L$  are the redshift and the luminosity distance of SBGs.  $R_{\text{SBN}}$  is the radius of the SBN.  $n_{\text{SBN}}$  and  $\mathcal{R}_{\text{SN}}$  are the gas number density and the SN rate in the SBN.  $v_{\text{SBNwind}}$  is the escaping speed of SBN superwind. The values are from Peretti et al. (2019).

<sup>b</sup>  $H_{\text{gas}}$  is the gas scale height.  $M_{\text{A,turb}}$  and  $v_{\text{Ai}}$  are the Alfvén Mach number of turbulence and the ion Alfvén speed. The values are from Krumholz et al. (2020).

<sup>c</sup>  $\mathcal{L}_{\text{SN}}$  and  $\mathcal{L}_{\text{SW}}$  are the amount of energy ejected per second by SN explosions and SWs in the SBN.  $\mathcal{L}_{\text{SN}}$  is estimated using  $\mathcal{R}_{\text{SN}}$ .  $\mathcal{L}_{\text{SW}}$  is estimated by us (see the text).

the injection of thermal particles to Fermi-I acceleration process, the magnetic field amplification due to resonant and non-resonant CR streaming instabilities, the drift of scattering centers relative to the underlying plasma, the escape of highest energy particles due to lack of resonant scattering waves, and the precursor heating due to wave damping (e.g., Ptuskin & Zirakashvili 2005; Vladimirov et al. 2008; Caprioli et al. 2009; Zirakashvili & Ptuskin 2012; Kang 2012).

In the test-particle regime, the DSA theory predicts that CRPs accelerated via Fermi-I process have the PL momentum spectrum whose slope is determined by the velocity jump of scattering centers across the shock (Bell 1978):

$$\alpha = \frac{3(u_1 + u_{w1})}{(u_1 + u_{w1}) - (u_2 + u_{w2})}, \quad (1)$$

where  $u_1$  and  $u_2$  are the bulk flow speeds in the shock rest frame, while  $u_{w1}$  and  $u_{w2}$  are the mean drift speeds of scattering centers relative to the underlying flows. Hereafter, we use the subscripts 1 and 2 to denote the preshock and postshock states, respectively. This slope could be greater than the slope estimated with the flow speeds only,  $q = 3u_1/(u_1 - u_2)$  (quoted in the introduction), since the scattering centers are likely to drift away from the spherically expanding SNR shock in both the preshock and postshock regions with speeds similar

to the local Alfvén speeds. For example,  $u_{w1} \sim -v_{A1}$  and  $u_{w2} \sim +v_{A2}$  (but note that  $u_{w2} \approx 0$  for isotropic turbulence in the downstream flow) (e.g. Berezhko & Völk 2000; Kang & Ryu 2010; Kang 2012), and then the Alfvénic drift of scattering centers tends to steepen the test-particle spectrum (e.g. Kang & Ryu 2018). The drift speed of scattering centers depends on the magnetic fields in the underling plasma, while the amplification of turbulent magnetic fields due to CR streaming instabilities depends on the CR acceleration efficiency, which in turn is controlled by the injection rate (Caprioli et al. 2009; Kang 2013). The full understanding of such nonlinear interdependence among the different plasma processes still remains quite challenging.

In the nonlinear DSA theory, on the other hand, the concavity in the CRP spectrum arises due to the development of a smooth precursor upstream of the subshock (e.g., Kang & Jones 2007; Caprioli et al. 2009). Then, low energy CRPs with shorter diffusion lengths experience smaller velocity jumps across the subshock, whereas higher energy CRPs with longer diffusion lengths feel larger velocity jumps across the total shock structure. As a result, the slope becomes  $\alpha_{\text{sub}} > \alpha$  (steeper) at the low energy part of the CRP spectrum, while it becomes  $\alpha_{\text{tot}} < \alpha$  (flatter) at the high energy part. Here,  $\alpha_{\text{sub}}$  ( $\alpha_{\text{tot}}$ ) is estimated by Equation (1) with the velocity jump across the subshock (total shock) transition. Obviously, this nonlinear feedback can be substantial for strong SNR shocks with high acceleration efficiencies, although the predicted efficiencies depend on the phenomenological models for the various processes adopted in numerical studies (e.g., Berezhko & Ellison 1999; Vladimirov et al. 2008; Bykov et al. 2014; Caprioli et al. 2010; Kang 2013). In the case of spherically expanding SNRs, however, the cumulative CRP spectrum integrated during the SNR evolution may exhibit only a mild concavity, as mentioned in the introduction.

Another critical issue is the highest energy of CRPs,  $E_{\text{max}} = p_{\text{max}}c$ , accelerated by blast waves from core-collapse SNe. SNRs propagate into slow red-supergiant (RSG) winds in the case of Type II or fast Wolf-Rayet (WR) winds in the case of Type Ib/c, before they run into the main-sequence (MS) wind shells (Berezhko & Völk 2000; Georgy et al. 2013). For instance, WR winds are metal-enriched and have strong magnetic fields, and the maximum energy of CR nuclei accelerated by such shocks could reach well above PeV. In addition, the blast waves do not decelerate significantly in the  $\rho \propto r^{-2}$  wind flows, the magnetic fields of SWs are stronger than the mean ISM fields, and the shock geometry is likely to be quasi-perpendicular due to the Parker-spiral magnetic field lines originating from the stellar surface

(e.g., Ptuskin & Zirakashvili 2005; Tatischeff 2009; Zirakashvili & Ptuskin 2016, 2018). Considering uncertainties in  $p_{\text{max}}$ , we here adopt  $p_{\text{max}} \simeq 1 - 100 \text{ PeV}/c$ , based on previous numerical studies.

## 2.2. Cosmic-Ray Production at Supernova Remnant Shocks

In order to take account of nonlinear effects, we consider double (broken) PL momentum spectra, in addition to single PL spectra, for CRPs produced by the collective SN explosions inside the SBN. First, the single PL form for the CRP production rate is given as

$$\mathcal{N}_{\text{SN},p}(p) \propto \left(\frac{p}{m_p c}\right)^{-\alpha_{\text{SN}}} \exp\left(-\frac{p}{p_{\text{max}}}\right) \quad (2)$$

with an exponential cutoff at  $p_{\text{max}}$ . Here, the slope  $\alpha_{\text{SN}}$  and  $p_{\text{max}}$  are free parameters. We adopt  $\alpha_{\text{SN}} \simeq 4.2 - 4.5$ , which is consistent with the range of values previously used for the modeling of  $\gamma$ -ray observations in the energy range of  $E_\gamma \lesssim 100 \text{ GeV}$  (e.g., Tamborra et al. 2014; Peretti et al. 2019).

The double PL form for the CRP production rate is modeled as

$$\mathcal{N}_{\text{SN},p}(p) \propto \begin{cases} \left(\frac{p}{m_p c}\right)^{-\alpha_{\text{SN},1}} & (p < p_{\text{brk}}) \\ \left(\frac{p}{m_p c}\right)^{-\alpha_{\text{SN},2}} \exp\left(-\frac{p}{p_{\text{max}}}\right) & (p \geq p_{\text{brk}}), \end{cases} \quad (3)$$

where  $p_{\text{brk}}$  is the break momentum between the two PLs. For a typical concave CRP spectrum integrated over the SNR age,  $\alpha_{\text{SN},2}$  is expected to be slightly smaller than  $\alpha_{\text{SN},1}$ , while  $p_{\text{brk}} \approx 10^{-3} - 10^{-2} p_{\text{max}}$  (Berezhko & Völk 2000; Tatischeff 2009; Kang 2013; Zirakashvili & Ptuskin 2016). We choose  $\alpha_{\text{SN},1} \simeq 4.2 - 4.5$  and  $\alpha_{\text{SN},2} \simeq 3.95 - 4.1$ . Here,  $\mathcal{N}_{\text{SN},p}(p)$  represents the CRP spectrum due to an ensemble of SNRs from different types of core-collapse SNe at different dynamical stages, and  $\int 4\pi p^2 \mathcal{N}_{\text{SN},p}(p) dp$  gives the volume-integrated CRP production rate in the entire volume of the SBN.

The normalization of the single and double PL momentum distributions in Equations (2) and (3) is fixed by the following condition:

$$\int_0^\infty 4\pi p^2 \mathcal{N}_{\text{SN},p}(p) [\sqrt{p^2 c^2 + m_p^2 c^4} - m_p c^2] dp = \eta_{\text{CR}} \mathcal{L}_{\text{SN}}. \quad (4)$$

Here, the amount of energy ejected per second by collective SN explosions in the SBN is given as  $\mathcal{L}_{\text{SN}} = \mathcal{R}_{\text{SN}} \times E_{\text{SN}}$  [erg s<sup>-1</sup>], where  $\mathcal{R}_{\text{SN}}$  is the SN rate and  $E_{\text{SN}}$  is the supernova explosion energy. We adopt the values of  $\mathcal{R}_{\text{SN}}$  given in Table 3 of Peretti et al. (2019). Assuming the mean explosion energy of  $E_{\text{SN}} = 10^{51} \text{ erg}$ , the estimated values of  $\mathcal{L}_{\text{SN}}$  are listed for three nearby

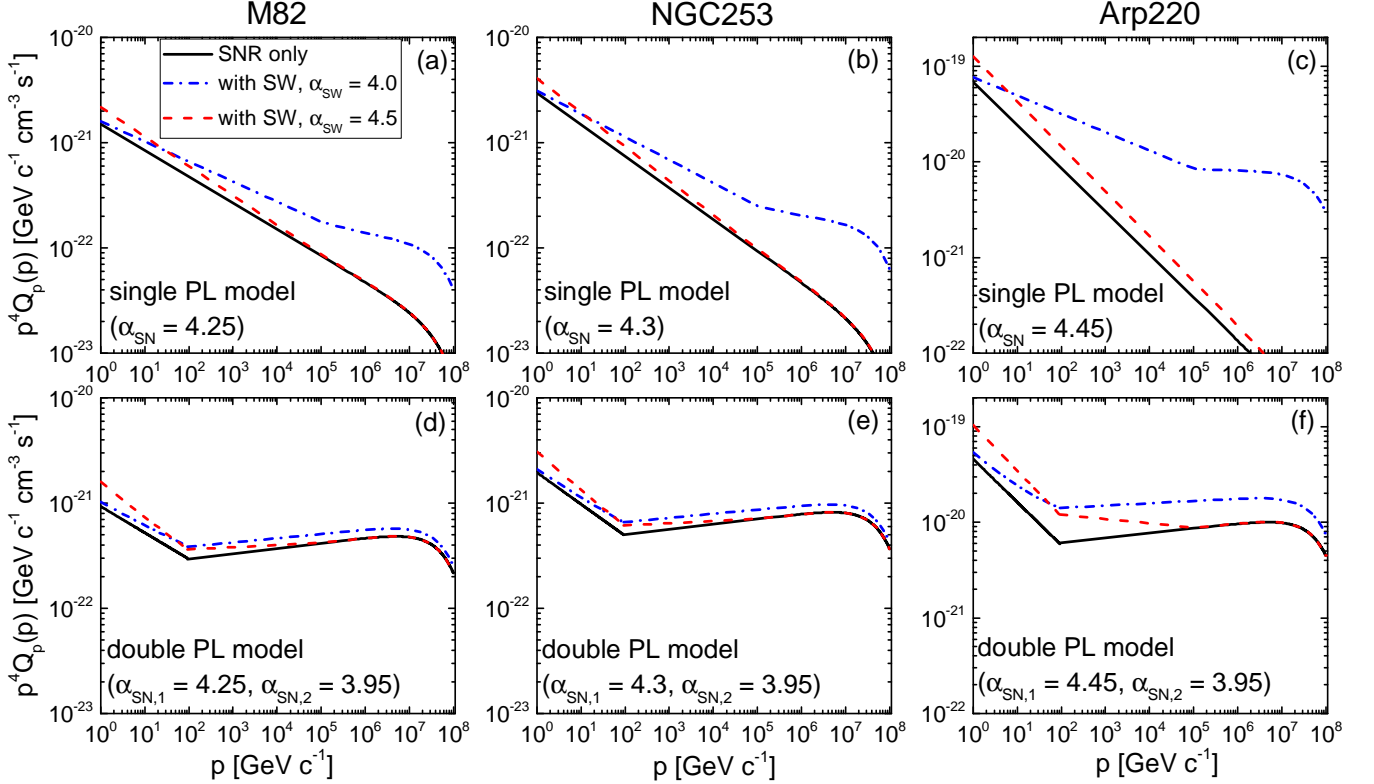


**Figure 2.** Injection rate of CRPs  $Q_p(p)$ , as a function of the CRP momentum, in the SBN for three nearby SBGs. The black solid lines show  $Q_p(p)$  of SNR-produced CRPs only, which are modeled with either single PL distributions (top panels) or double PL distributions with  $p_{\text{brk}} = 10^2 m_p c$  (bottom panels). The adopted PL slopes are given in each panel. The red dashed lines and blue dashed-dot lines show  $Q_p(p)$  that includes additional SW-produced CRPs, which are modeled with single PL distributions. Two different PL slopes,  $\alpha_{\text{sw}} = 4.0$  and  $4.5$ , are considered. In all model distributions,  $p_{\text{max}} = 100 \text{ PeV}/c$  is used.

SBGs in Table 1. The mean acceleration efficiency of CRPs at SNRs is taken as  $\eta_{\text{CR}} \simeq 0.1$  (e.g., [Caprioli & Spitkovsky 2014](#)).

### 2.3. Mechanical Energy Deposition by Stellar Winds

The current understanding of stellar evolution indicates that massive stars with the initial mass of  $12M_\odot \lesssim M_{\text{ZAMS}} \lesssim 35M_\odot$  eject the MS wind, followed by the RSG wind, before they explode as Type II SNe. (Here, ZAMS stands for zero-age main sequence.) More massive stars with  $M_{\text{ZAMS}} \gtrsim 35M_\odot$  expel the MS wind, followed by the WR wind, before they explode as Type Ib/c SN ([Georgy et al. 2013](#)). Adopting an IGIMF for our Galaxy and the SN explosion rate of  $\mathcal{R}_{\text{SN}} = 0.015 \text{ yr}^{-1}$ , [Seo et al. \(2018\)](#) estimated that the total wind luminosity emitted by all massive stars in the Galactic disk is about  $\mathcal{L}_w \approx 1/4 \mathcal{L}_{\text{SN}}$  in the Milky Way.

To estimate the galaxy-wide wind luminosity,  $\mathcal{L}_w$ , in the SBN of three nearby SBGs in Table 1, we follow the prescription given in [Seo et al. \(2018\)](#), which will be described briefly here without repeating all the details. The first step is to estimate the mass function,  $N(m) = A_{\text{OB}} m^{-\beta}$ , of all stars with the initial mass,

$m$ , contained in the SBN, where the slope  $\beta$  depends on the SFR ([Palla et al. 2020](#)) and the normalization factor  $A_{\text{OB}}$  is determined by  $\mathcal{R}_{\text{SN}}$  of each SBG. For M82 and NGC253, the SFR is  $\lesssim 10 M_\odot \text{ yr}^{-1}$ , so  $\beta \sim 2.35$  is used. Arp220, on the other hand, has a higher SFR,  $\gtrsim 100 M_\odot \text{ yr}^{-1}$ , so a flatter slope,  $\beta \sim 1$ , is adopted. We then estimate the mass function,  $N_k(m)$ , in the  $k$ -th wind stage, which represents the MS, RSG, or WR stage, using Equation (32) of [Seo et al. \(2018\)](#). The wind mechanical luminosity at each wind stage,  $L_k(M) = 1/2 \dot{M}_k v_{\text{SW},k}^2$ , are calculated using their Equations (24)-(28), where  $M$  is the stellar mass at a given stage. The fitting forms for the mass loss rate,  $\dot{M}_k$ , and the wind velocity,  $v_{\text{SW},k}$ , derived from observational and theoretical estimations, were given in their paper. Note that the conversion of  $L_k(M)$  to the wind luminosity as a function of the initial mass  $m$ ,  $L_k(m)$ , requires the estimation of  $M$  through numerical calculations of stellar evolutionary tracks (e.g., [Ekström et al. 2012](#); [Georgy et al. 2013](#)). Finally, the galaxy-wide wind luminosity is calculated as

$$\mathcal{L}_{\text{SW}} = \sum_k \int N_k(m) L_k(m) dm, \quad (5)$$

where the index  $k$  is for the three wind stages, and the mass range (in units of  $M_\odot$ ) of each integral is  $[10, 150]$  for the MS stage,  $[10, 40]$  for the RSG stage, and  $[25, 150]$  for the WR stage.

Note that the SN contribution is more important compared to that of the SW contribution:  $\mathcal{L}_{\text{SW}}/\mathcal{L}_{\text{SN}} \sim 0.3$  for M82 and NGC253, but  $\mathcal{L}_{\text{SW}}/\mathcal{L}_{\text{SN}} \sim 0.87$  for Arp220. In our model, for a higher SFR, the slope  $\beta$  of the IGIMF is flatter (Palla et al. 2020), resulting in a larger contribution to  $\mathcal{L}_{\text{SW}}$  from more massive stars. Hence, SBGs with higher SFRs have relatively larger SW contributions with respect to SN contribution.

#### 2.4. Cosmic-Ray Production at Stellar Wind Shocks

Pre-SN winds are known to induce several kinds of shocks, including termination shocks in the wind flow, forward shocks around the wind bubble, colliding-wind shocks in massive binaries, and bow-shocks of massive runaway stars. Most of the mechanical energy of fast stellar winds is expected to be dissipated at strong termination shocks during the MS and WR stages. For typical SWs of O-type MS and WR stars, the wind termination velocity ranges  $v_{\text{SW}} \sim 1 - 3 \times 10^3 \text{ km s}^{-1}$ , and the temperature of the wind flow ranges  $T_{\text{SW}} \sim 10^4 - 10^5 \text{ K}$  (Georgy et al. 2013), so the termination shock is expected to have high Mach numbers and the nonlinear DSA might be important there. However, the details of DSA physics at SW shocks are rather poorly understood, compared to those at SNRs. For example, the Alfvénic drift effects due to amplified turbulent magnetic fields are somewhat uncertain, because the magnetic fields are inferred to be strong with quasi-perpendicular configuration at the termination shock. Moreover, the quantitative calculation of nonlinear DSA at such termination shocks or forward shocks around the wind bubble has not been made so far, unlike in the case of SNRs.

Considering the lack of clear understanding of nonlinear DSA physics and also the CRP contributions from several types of shocks mentioned above, for the sake of simplicity, we assume that the cumulative, time-integrated spectra of CRPs produced by SWs is represented by the single PL form, and that the DSA efficiency is similar to the widely adopted value for SNRs,  $\eta_{\text{CR}} \sim 0.1$ . Hence, the CRPs production rate due to the collection of shocks induced by SWs from an ensemble of massive stars in the SBN is modeled as

$$\mathcal{N}_{\text{SW},p}(p) \propto \left(\frac{p}{m_p c}\right)^{-\alpha_{\text{SW}}} \exp\left(-\frac{p}{p_{\text{max}}}\right), \quad (6)$$

where we adopt  $\alpha_{\text{SW}} \simeq 4.0 - 4.5$  and  $p_{\text{max}} \sim 1 - 100 \text{ PeV}/c$ , similarly as in  $\mathcal{N}_{\text{SN},p}(p)$ . Again, the normalization for  $\mathcal{N}_{\text{SW},p}$  for each SBG is fixed by the following

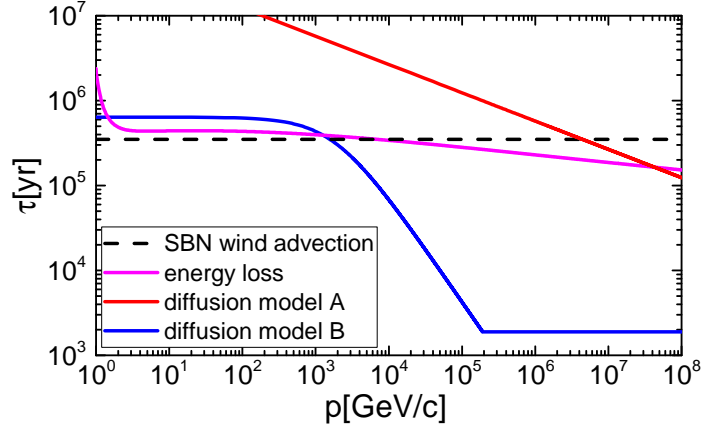


**Figure 3.** Timescales in the modeling of CRP transport due to the energy loss, SBN wind advection, and turbulent diffusion for M82. In the diffusion model A, CRPs are assumed to scatter off large-scale, Kolmogorov turbulence. In the diffusion model B, CRPs interact with self-excited Alfvén waves. The line of the model B is for the single PL momentum distribution of SNR-produced CRPs only with  $\alpha_{\text{SN}} = 4.25$  (the black line in Figure 2(a)), and the kink around  $p \sim 0.1 \text{ PeV}/c$  is caused by the limit of streaming speed,  $v_{\text{st}} < c$ .

relation

$$\int_0^\infty 4\pi p^2 \mathcal{N}_{\text{SW},p}(p) [\sqrt{p^2 c^2 + m_p^2 c^4} - m_p c^2] dp = \eta_{\text{CR}} \mathcal{L}_{\text{SW}}, \quad (7)$$

with  $\mathcal{L}_{\text{SW}}$  in Table 1.

#### 2.5. Combined Cosmic-Ray Productions

Using  $\mathcal{N}_{\text{SN},p}(p)$  and  $\mathcal{N}_{\text{SW},p}(p)$ , we define the CRP injection rate in the SBN as

$$Q_p(p) = \frac{\mathcal{N}_{\text{SN},p}(p) + \mathcal{N}_{\text{SW},p}(p)}{V}, \quad (8)$$

where  $V$  is the volume of the SBN, calculated with  $R_{\text{SBN}}$  in Table 1. We have two CRP production models, (1) the single PL model, in which both the SNR and SW-produced CRPs follow single PL distributions, and (2) the double PL model, in which the SNR-produced CRPs follow double PL distributions while the SW-produced CRPs follow single PL distributions.

Figure 2 compares  $Q_p(p)$  of three nearby SBGs for the two CRP production models (single versus double PL) with two different slopes of SW-produced CRPs ( $\alpha_{\text{SW}} = 4.0$  and  $4.5$ ). The consequence of the double PL model is obvious, especially in the high-momentum range. For M82, for instance,  $Q_p(p)$  of the double PL model (panel (d)) is several to ten times larger than that of the single PL model (panel (a)) for  $p \gtrsim 0.1 \text{ PeV}/c$ . This implies that the flux of high energy neutrinos of  $E_\nu \gtrsim 10 \text{ TeV}$  would be larger with the double PL model (see Section

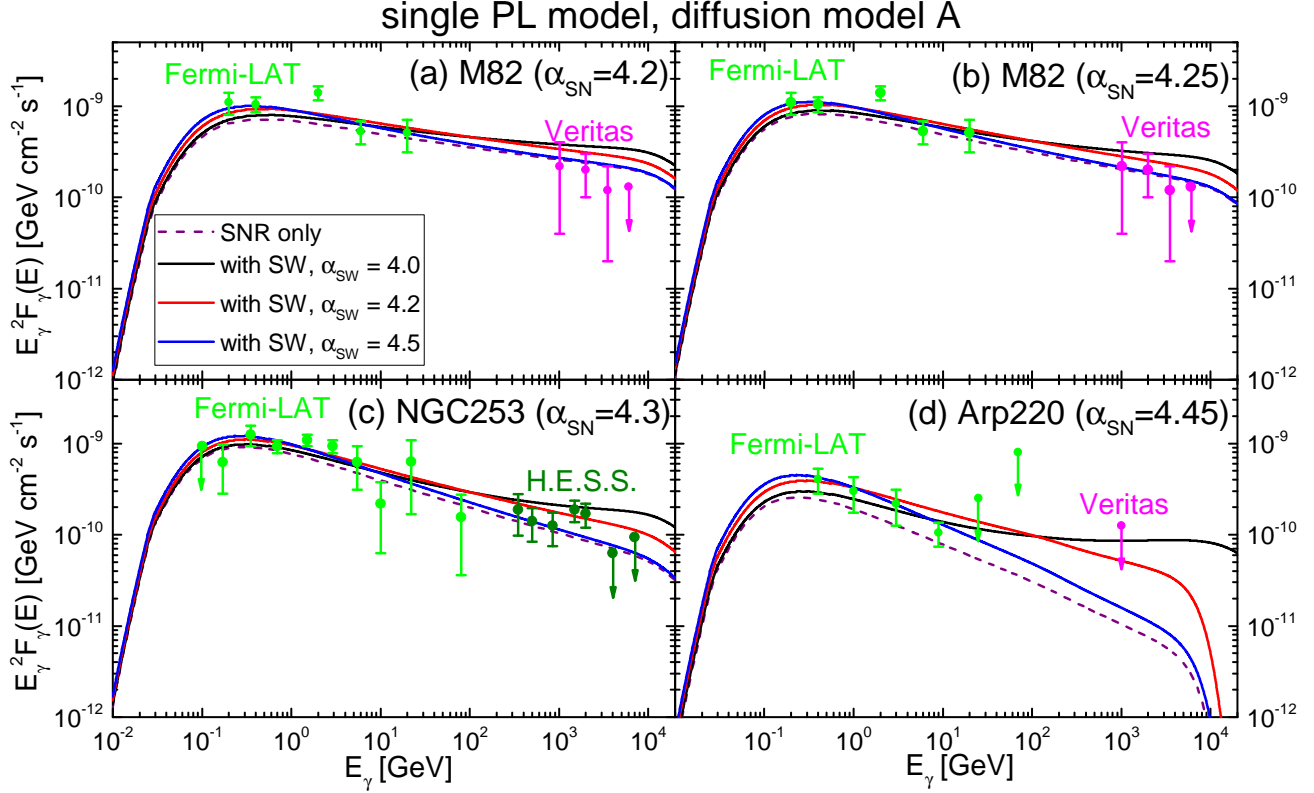


**Figure 4.** Estimated  $\gamma$ -ray fluxes for M82 in (a) and (b), NGC253 in (c), and Arp220 (d). The SNR-produced CRPs are modeled with single PL momentum distributions, where the slopes are the best fitted values quoted in Peretti et al. (2019, 2020). The SW-produced CRPs are also modeled with single PL momentum distributions, but with a number of different slopes. Here,  $p_{\max} = 100$  PeV/c is used in both the SNR and SW-produced CRP distributions. The value of  $p_{\max}$  is not important in the  $\gamma$ -ray energy range shown, due to the attenuation against the extragalactic background photons, and the results remain the same for  $p_{\max} = 1$  PeV/c (and also in the following Figures 5 to 7). For turbulent diffusion, the model A is used. Observation data (dots with error bars) are shown for comparison. For M82, the Fermi-LAT data are from Acero et al. (2015) and the Veritas data are from VERITAS Collaboration et al. (2009). For NGC253, both Fermi-LAT and H.E.S.S. data are from H. E. S. S. Collaboration et al. (2018). For Arp220, the Fermi-LAT data are from Peng et al. (2016) and the upper limit by Veritas is from The VERITAS Collaboration et al. (2015). (The same observation data are shown in the following Figures 5 to 7.)

5). With a flat spectrum, such as  $\alpha_{\text{SW}} \simeq 4.0$ , the SW-produced CRPs could substantially contribute to  $Q_p(p)$  over a wide momentum range. Especially, in Arp220 where the SFR is high, the SW contribution could be quite important, especially at high momenta. On the other hand, with a steeper spectrum, such as  $\alpha_{\text{SW}} \simeq 4.5$ , the SW contribution should be less noticeable.

### 3. MODELS FOR COSMIC-RAY TRANSPORT

Following the simple approach adopted in previous studies (referenced in the introduction), we assume that the production of CRPs is balanced by the energy loss, SBN wind advection, and diffusion. Then, the momentum spectrum of the CRP density in the SBN,  $f_p(p)$ , is given as

$$\frac{f_p(p)}{\tau_{\text{loss}}} + \frac{f_p(p)}{\tau_{\text{adv}}} + \frac{f_p(p)}{\tau_{\text{diff}}} = Q_p(p). \quad (9)$$

The energy loss is mostly due to ionization, Coulomb collisions, and inelastic  $pp$  collisions, and for its timescale  $\tau_{\text{loss}}$ , we use the formulae in Peretti et al. (2019). The wind advection timescale  $\tau_{\text{adv}}$  is calculated as the radius of the SBN divided by the escaping speed of the SBN wind, i.e.,  $R_{\text{SBN}}/v_{\text{SBNwind}}$  with  $R_{\text{SBN}}$  and  $v_{\text{SBNwind}}$  in Table 1. Figure 3 shows  $\tau_{\text{loss}}$  (magenta solid line) and  $\tau_{\text{adv}}$  (black dashed line) estimated for M82; the two time scale are comparable.

For the diffusion timescale  $\tau_{\text{diff}}$ , we consider two different diffusion models. First, we adopt the model A of Peretti et al. (2019), where CRPs scatter off the large-scale Kolmogorov turbulence in the SBN (hereafter, the diffusion model A). Then, the diffusion coefficient is given as

$$D_A(p) \approx \frac{r_g(p)c}{3\mathcal{F}(k)}, \quad (10)$$

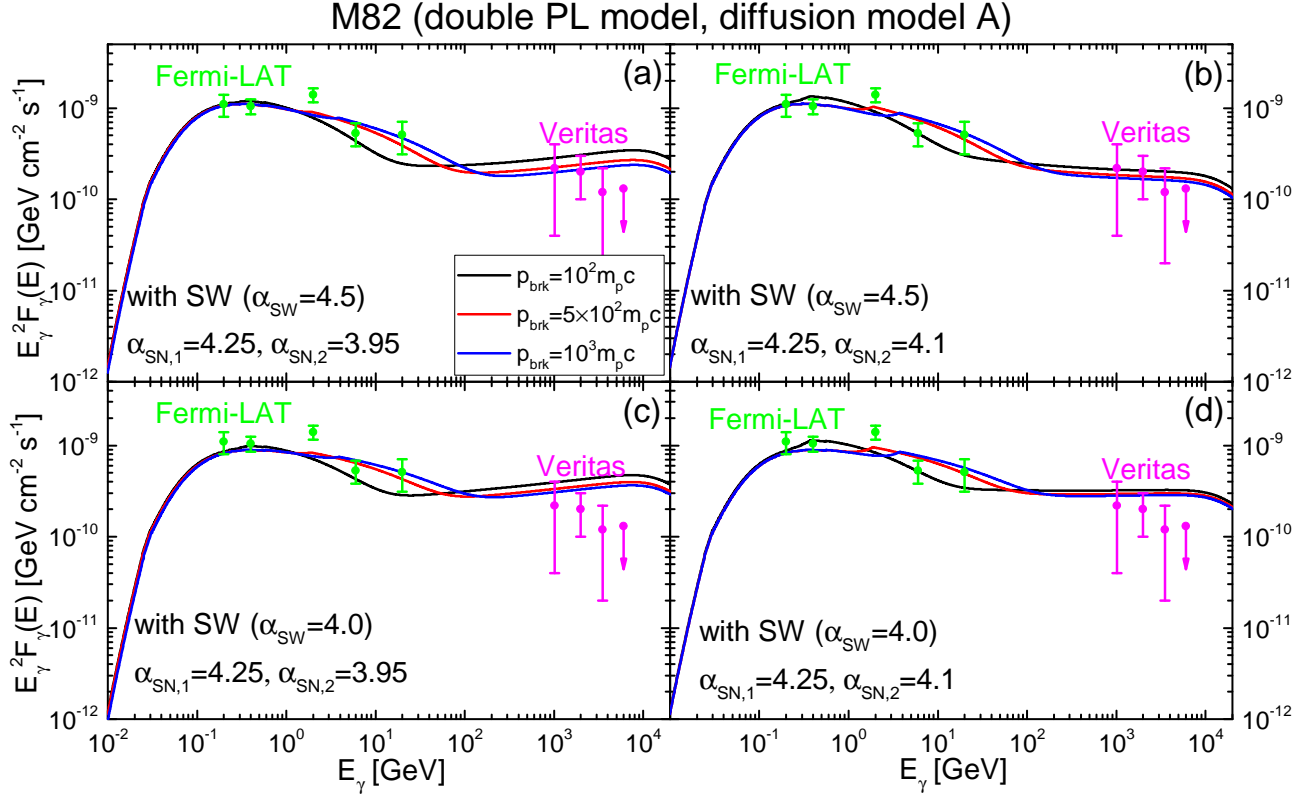


**Figure 5.** Comparison of estimated  $\gamma$ -ray fluxes with observed data (dots with error bars) for M82 using different CRP distributions. The SNR-produced CRPs are modeled with double PL momentum distributions, while the SW-produced CRPs are modeled with single PL momentum distributions. Here,  $p_{\max} = 100$  PeV/ $c$  and  $p_{\text{brk}} = 10^2 m_p c$  for both the SNR and SW-produced CRP distributions. For turbulent diffusion, the model A is used.

where  $r_g(p)$  is the gyroradius of CRPs and the speed of CRPs is assumed to be  $c$ .  $\mathcal{F}(k)$  is the normalized energy density of turbulent magnetic fields per unit logarithmic wavenumber, which is defined as

$$\int_{k_0}^{\infty} \mathcal{F}(k) \frac{dk}{k} = \left( \frac{\delta B_{\text{SBN}}}{B_{\text{SBN}}} \right)^2 = 1 \quad (11)$$

with  $k_0 = 1 \text{ pc}^{-1}$ . Note that 1 pc is about the gyroradius of CRP of 100 PeV in the background magnetic field of 100  $\mu\text{G}$ . The diffusion timescale is given as  $\tau_{\text{diff}} = R_{\text{SBN}}^2 / D_A(p)$  with the radius of the SBN. We point that  $r_g(p) \propto p$ , and  $\mathcal{F}(k) \propto k^{-2/3} \propto p^{2/3}$  assuming that CRPs interact with the resonant mode corresponding to the gyroradius, and then  $\tau_{\text{diff}} \propto p^{-1/3}$ . Peretti et al. (2019) also considered the Bohm diffusion, for which  $D(p) \sim r_g(p)c \propto p$  and  $\tau_{\text{diff}} \propto p^{-1}$ . But they argue that the Bohm diffusion essentially gives the same results as the Kolmogorov diffusion for the transport of CRPs, because the SBN wind advection has a shorter timescale over most of the momentum range (see Figure 3) and so those diffusions are subdominant. Hence, we here consider only the Kolmogorov turbulence for the diffusion model A.

We also consider the diffusion model of Krumholz et al. (2020), where CRPs of  $E_{\text{CR}} \lesssim 0.1$  PeV resonantly scatter off self-excited turbulence (hereafter, the diffusion model B). Assuming that the turbulence is trans or super-Alfvénic, the diffusion coefficient is given as

$$D_B(p) \approx v_{\text{st}} \ell, \quad (12)$$

where  $v_{\text{st}}$  is the CRP streaming speed, and  $\ell \approx \ell_0 / M_{\text{A,turb}}^3$ ,  $\ell_0$  is the outer scale of the turbulence, and  $M_{\text{A,turb}}$  is the Alfvén Mach number of the turbulence. Following Krumholz et al. (2020),  $\ell_0 = H_{\text{gas}}$ , i.e., the gas scale height listed in Table 1, is used, and  $M_{\text{A,turb}} = 2$  is assumed. And  $v_{\text{st}}$  is modeled as  $(v_{\text{st}}/v_{\text{Ai}} - 1) \propto (E_{\text{CR}}/\text{GeV})^{\alpha-3}$ , where  $v_{\text{Ai}}$  is the ion Alfvén speed given in Table 1 and  $\alpha$  is the PL slope of CRP momentum distribution,  $\alpha_{\text{SN}}$  or  $\alpha_{\text{SW}}$ , described in Section 2. The proportional constant for different SBGs can be found in Table 1 of Krumholz et al. (2020). The diffusion timescale is given as  $\tau_{\text{diff}} = H_{\text{gas}}^2 / D_B(p) = M_{\text{A,turb}}^3 H_{\text{gas}} / v_{\text{st}}$ .

Figure 3 compares  $\tau_{\text{diff}}$  to  $\tau_{\text{loss}}$  and  $\tau_{\text{adv}}$  for M82. In the estimation of  $\tau_{\text{diff}}$  of the diffusion model B in the figure (blue solid line), the single PL momentum distribution of SNR-produced CRPs only with  $\alpha_{\text{SN}} = 4.25$  is

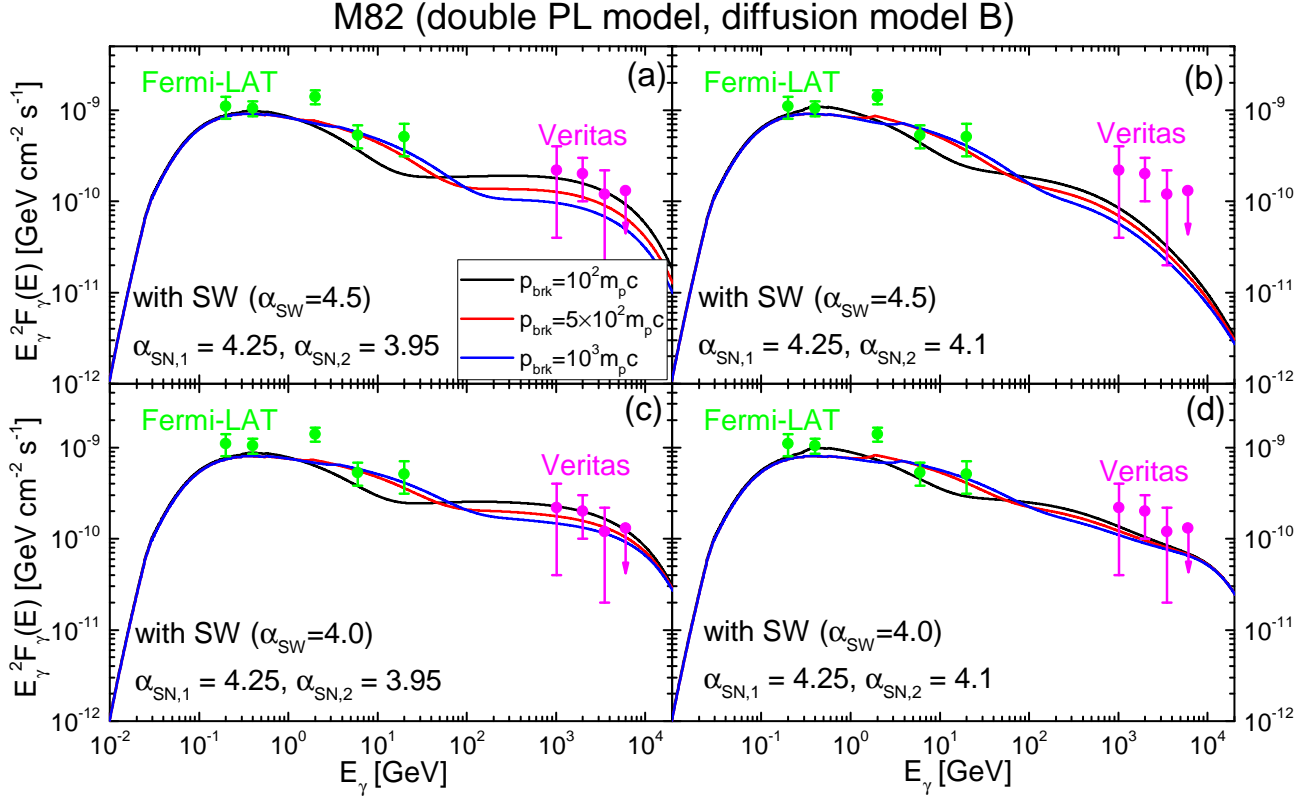


**Figure 6.** Same as in Fig. 5, except using the diffusion model B.

used. The slope of  $\tau_{\text{diff}}(p)$  in the range of  $p \sim 1 - 100$  TeV/c is  $3 - \alpha_{\text{SN}}$ . With the diffusion model A, the energy loss and wind advection dominate over the turbulent transport, except at the highest momentum of  $p \gtrsim 10$  PeV/c. In the case of the diffusion model B, on the other hand,  $\tau_{\text{diff}}$  becomes shorter than  $\tau_{\text{loss}}$  or  $\tau_{\text{adv}}$  for  $p \gtrsim 1$  TeV/c, so high energy CRPs are confined within the SBN for shorter time and have less chance for collisions with background thermal protons. The kink in  $\tau_{\text{diff}}$  of the diffusion model B appears at  $p \sim 0.1$  PeV/c, because the momentum-dependent streaming velocity becomes greater than the speed of light. Hence, the model stops being valid at  $p \gtrsim 0.1$  PeV/c; the CRPs in the momentum range may interact with the large-scale turbulence in the SBN, resulting in longer  $\tau_{\text{diff}}$ . This may affect in particular the estimation of neutrino emission in  $E_\nu \gtrsim 10$  TeV (see Section 5 for further comments).

#### 4. GAMMA-RAY EMISSION FROM SBGS

With the CRP momentum distribution function,  $f_p(p)$ , calculated in Equation (9), we first estimate the  $\gamma$ -ray emission due to  $pp$  collisions. As in previous studies, we use the pion source function as a function of pion

energy  $E_\pi$ , presented in Kelner et al. (2006),

$$q_\pi(E_\pi) = \frac{cn_{\text{SBN}}}{K_\pi} \sigma_{pp} \left( m_p c^2 + \frac{E_\pi}{K_\pi} \right) n_p \left( m_p c^2 + \frac{E_\pi}{K_\pi} \right). \quad (13)$$

Here,  $K_\pi \sim 0.17$  is the fraction of the kinetic energy transferred from proton to pion, and  $n_p(E)$  is the CRP energy distribution, given as  $n_p(E)dE = 4\pi p^2 f_p(p)dp$ . And  $\sigma_{pp}(E)$  is the cross-section, given as  $(34.3 + 1.88\theta + 0.25\theta^2) \times [1 - (E_{\text{th}}/E)^4]^2$  mb, where  $\theta = \ln(E/\text{TeV})$  and  $E_{\text{th}} = 1.22$  GeV is the threshold energy. The  $\gamma$ -ray source function as a function of  $\gamma$ -ray energy  $E_\gamma$  is calculated as

$$q_\gamma(E_\gamma) = 2 \int_{E_{\text{min}}}^{\infty} \frac{q_\pi(E_\pi)}{\sqrt{E_\pi^2 - m_\pi^2 c^4}} dE_\pi, \quad (14)$$

where  $E_{\text{min}} = E_\gamma + m_\pi^2 c^4 / (4E_\gamma)$ . Then, the  $\gamma$ -ray flux as a function of  $E_\gamma$  is calculated as

$$F_\gamma(E_\gamma) = \frac{q_\gamma(E_\gamma)V}{4\pi D_L^2} \exp[-\tau_{\gamma\gamma}(E_\gamma, z)], \quad (15)$$

where  $D_L$  is the luminosity distance of SBGs in Table 1. Here, the optical depth,  $\tau_{\gamma\gamma}$ , takes into account pair production with the background photons in both the SBN and intergalactic space, and we use the analytic approximation suggested by Peretti et al. (2019).

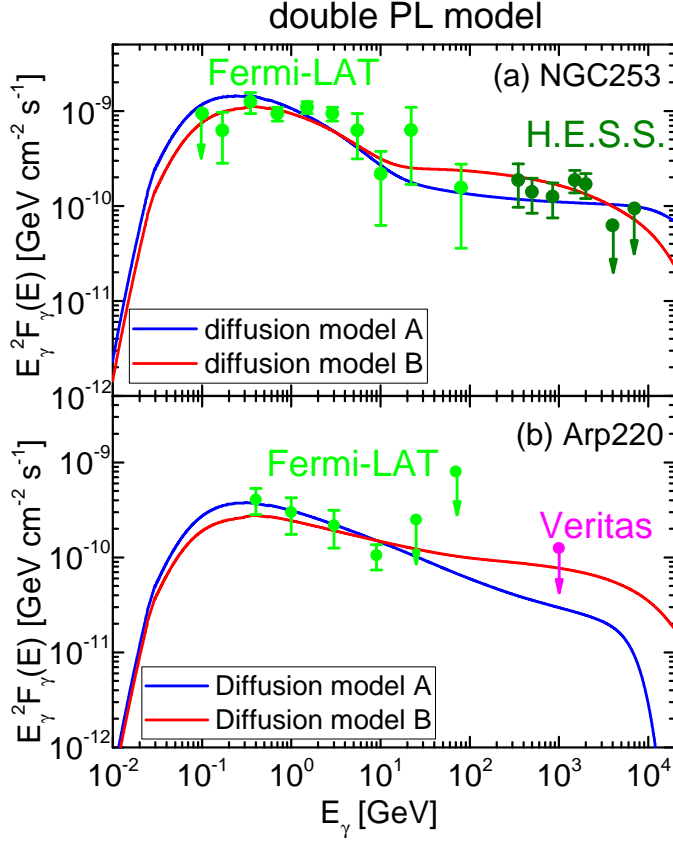


**Figure 7.** Comparison of estimated  $\gamma$ -ray fluxes with observed data (dots with error bars) for NGC253 in (a) and Arp220 in (b), using two different diffusion models. The SNR-produced CRPs are modeled with double PL momentum distributions, while the SW-produced CRPs are modeled with single PL momentum distributions, with the following slopes: for NGC253,  $\alpha_{\text{SN},1} = 4.3$ ,  $\alpha_{\text{SN},2} = 4.1$ ,  $\alpha_{\text{SW}} = 4.5$  (model A, blue line), and  $\alpha_{\text{SN},1} = 4.3$ ,  $\alpha_{\text{SN},2} = 3.95$ ,  $\alpha_{\text{SW}} = 4.0$  (model B, red line); for Arp220,  $\alpha_{\text{SN},1} = 4.45$ ,  $\alpha_{\text{SN},2} = 4.1$ ,  $\alpha_{\text{SW}} = 4.5$  (model A, blue line), and  $\alpha_{\text{SN},1} = 4.45$ ,  $\alpha_{\text{SN},2} = 3.95$ ,  $\alpha_{\text{SW}} = 4.0$  (model B, red line). Here,  $p_{\text{max}} = 100 \text{ PeV}/c$  and  $p_{\text{brk}} = 10^2 m_p c$  for both the SNR and SW-produced CRP distributions.

Figure 4 shows  $F_\gamma$  estimated with the single PL distributions for SNR-produced CRPs and SW-produced CRPs, along with the diffusion model A. The best fitted values of Peretti et al. (2019, 2020) are chosen for  $\alpha_{\text{SN}}$ , while different values are tried for  $\alpha_{\text{SW}}$ . The  $\gamma$ -ray observations of M82 and NGC253 are well reproduced; the contribution of SW CRPs is subdominant for those SBGs, as expected with  $\mathcal{L}_{\text{SW}} < \mathcal{L}_{\text{SN}}$  in Table 1. However, with  $\mathcal{L}_{\text{SW}} \sim \mathcal{L}_{\text{SN}}$  for Arp220, we argue that the contribution of SW CRPs could be important, especially, if  $\alpha_{\text{SW}}$  is small. For instance, with  $\alpha_{\text{SW}} = 4.0$ ,  $F_\gamma$  at  $E_\gamma \sim 1 \text{ TeV}$  approaches the upper limit of the Veritas observation. We point that with the diffusion model B, the single PL model for SNR CRPs predicts  $\gamma$ -ray

**Table 2.** Model Parameters for Best Reproduction of  $\gamma$ -ray Observations

	SNR CRPs	$\alpha_{\text{SN},1}(=\alpha_{\text{SN}})$	$\alpha_{\text{SN},2}$	$\alpha_{\text{SW}}$	diffusion
M82	single PL	4.25	-	4.5	A
NGC253	single PL	4.3	-	4.5	A
Arp220	single PL	4.45	-	4.5	A
M82	double PL	4.25	4.1	4.5	A
NGC253	double PL	4.3	4.1	4.5	A
Arp220	double PL	4.45	4.1	4.5	A
M82	double PL	4.25	3.95	4.0	B
NGC253	double PL	4.3	3.95	4.0	B
Arp220	double PL	4.45	3.95	4.0	B

$p_{\text{brk}} = 100 m_p c$  is used for the double PL distribution.

fluxes for the considered SBGs, which are too small to be consistent with Veritas and H.E.S.S. observations at  $E_\gamma \gtrsim \text{TeV}$ .

The  $\gamma$ -ray fluxes of M82 estimated with the double PL momentum distributions for SNR CRPs are shown in Figure 5 (with the diffusion model A) and Figure 6 (with the diffusion model B). The single PL momentum distributions with  $\alpha_{\text{SW}} = 4.0$  or  $4.5$  are employed for SW CRPs.  $F_\gamma$  in the energy range of  $E_\gamma \lesssim 100 \text{ GeV}$  is insensitive to the diffusion model since the transport of CRPs with  $p \lesssim 1 \text{ TeV}/c$  is controlled by the SBN wind advection. Hence, the Fermi-LAT data are reproduced for both of the diffusion models, if the slope of the low momentum part is adjusted, i.e.,  $\alpha_{\text{SN},1} = 4.25$ .  $F_\gamma$  in the higher energy range, on the other hand, is affected substantially by the diffusion model, because the transport timescale of CRPs with  $p \gtrsim 1 \text{ TeV}/c$  is much longer in the model A than in the model B, as shown in Figure 3. The reproduction of the Veritas data for  $E_\gamma \gtrsim 1 \text{ TeV}$  requires a softer spectrum in the high momentum part, for instance,  $\alpha_{\text{SN},2} = 4.1$  (e.g., Fig. 5(b)), in the case of the model A, while it requires a harder spectrum,  $\alpha_{\text{SN},2} = 3.95$  (e.g., Fig. 6(c)), in the case of the model B. Other model parameters involved are less important. Yet, somewhat better fittings are obtained with larger  $\alpha_{\text{SW}}$ , such as 4.5, if the diffusion model A is adopted, and with smaller  $\alpha_{\text{SW}}$ , such as 4.0, if the diffusion model B is adopted.  $p_{\text{brk}}$  affects the predicted fluxes at high energies, but with the adopted range of  $p_{\text{brk}} \simeq 10^2 - 10^3 m_p c$ , the difference in  $F_\gamma$  is at most a factor of two.

Figure 7 shows the  $\gamma$ -ray fluxes of NGC25 and Arp220 estimated with the double PL distributions for SNR CRPs. For  $\alpha_{\text{SN},1}$ , the values that reproduce the Fermi-

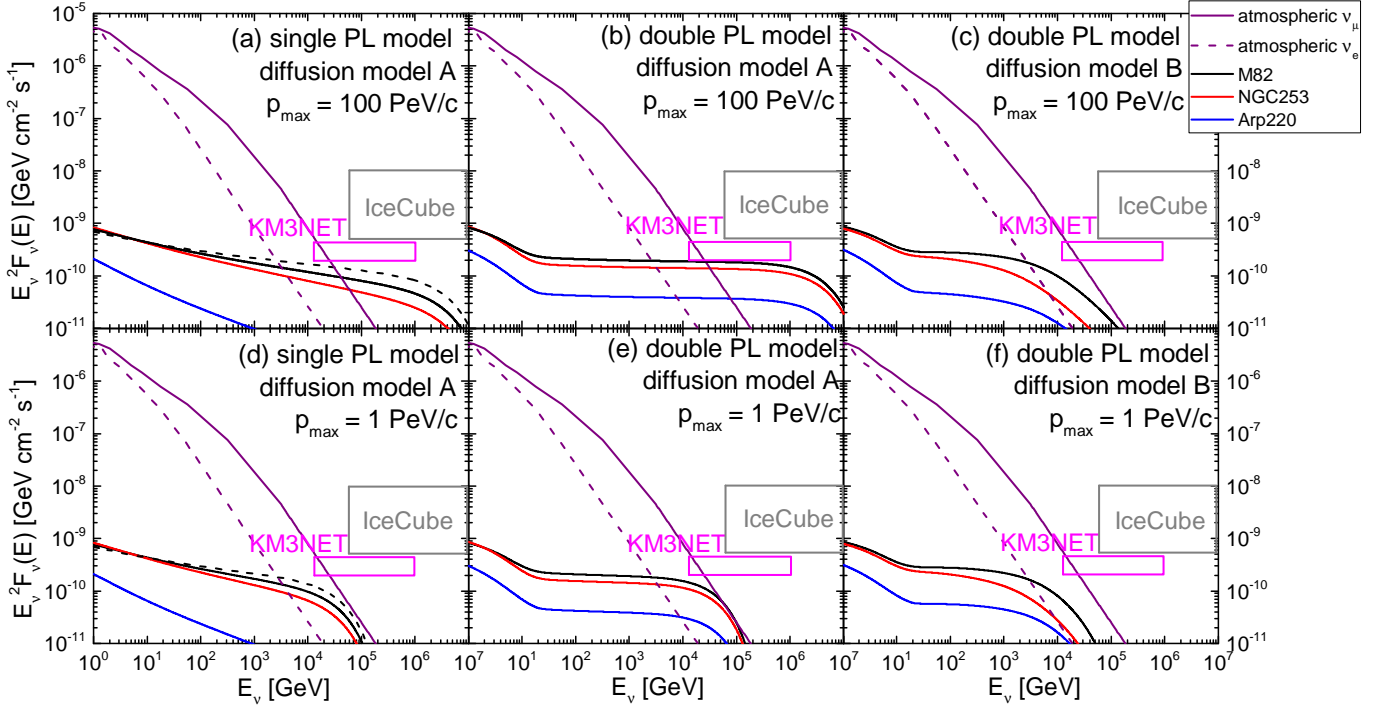


**Figure 8.** Predicted neutrino fluxes from three nearby SBGs with the model parameters listed in Table 2 (solid lines);  $p_{\max} = 100$  PeV/c (upper panels) and  $p_{\max} = 1$  PeV/c (lower panels) are used. In panels (a) and (d), the black solid line is for M82 with  $\alpha_{\text{SN}} = 4.25$ , while the black dashed line is with  $\alpha_{\text{SN}} = 4.2$ . The boxes draw the ranges of the IceCube point source sensitivity (Aartsen et al. 2017, grey) and the KM3NET point source sensitivity (Aiello et al. 2019, magenta) (see the text for details). The dark purple solid and dashed lines draw the fluxes of atmospheric muon and electron neutrinos from the data of Richard et al. (2016). The fluxes shown are within a circular beam of  $1^\circ$  diameter.

LAT data are used. Again, with the diffusion model A (blue lines), a softer distribution at the high momentum part with  $\alpha_{\text{SN},2} = 4.1$  reproduces the the H.E.S.S. and Veritas observations better, while with the diffusion model B (red lines), a harder distribution with  $\alpha_{\text{SN},2} = 3.95$  does better. The model parameters used are listed in the figure caption.

Overall, the best results for the reproduction of the  $\gamma$ -ray observations of three nearby SBGs are obtained with the combination of the double PL model for SNR CRPs and the diffusion model B. Table 2 lists the best fit parameters of the single PL model for SNR CRPs with the diffusion model A, and those of the double PL model for SNR CRPs with the diffusion models A and B. The combination of the single PL model for SNR CRPs and the diffusion model B does not produce satisfactory results, as mentioned above, so the parameters for the case are not listed.

## 5. NEUTRINO EMISSION FROM SBGS

We then predict the neutrino fluxes from three nearby SBGs with the model parameters listed in Table 2. We again employ the formulae presented in Kelner et al. (2006). The neutrino source function as a function of

neutrino energy  $E_\nu$  is given as

$$q_\nu(E_\nu) = 2 \int_0^1 \left[ f_{\nu_\mu^{(1)}}(x) + f_{\nu_\mu^{(2)}}(x) + f_{\nu_e}(x) \right] q_\pi \left( \frac{E_\nu}{x} \right) \frac{dx}{x}, \quad (16)$$

where  $x = E_\nu/E_\pi$ . The term  $f_{\nu_\mu^{(1)}}(x)$  represents the muon neutrino production through the pion decay  $\pi \rightarrow \mu\nu_\mu$ , and  $f_{\nu_\mu^{(2)}}(x)$  and  $f_{\nu_e}(x)$  describe the muon and electron neutrino productions through the muon decay  $\mu \rightarrow \nu_\mu\nu_e$ . The formulae for  $f_{\nu_\mu^{(1)}}$ ,  $f_{\nu_\mu^{(2)}}$ , and  $f_{\nu_e}$  are given in Kelner et al. (2006). Then, the neutrino flux observed at the Earth is calculated as

$$F_\nu(E_\nu) = \frac{q_\nu(E_\nu)V}{4\pi D_L^2}. \quad (17)$$

Figure 8 shows the predicted neutrino fluxes,  $F_\nu$ , for two values of the maximum momentum of CRP distributions,  $p_{\max} = 100$  PeV/c (upper panels) and  $p_{\max} = 1$  PeV/c (lower panels). We compare  $F_\nu$  to the point source sensitivity ranges of IceCube and KM3NET:  $E_\nu^2 F_\nu \sim 5 \times 10^{-10} - 10^{-8}$  GeV cm $^{-2}$ s $^{-1}$  in the energy range of  $E_\nu \gtrsim 60$  TeV for IceCube with seven-year data (Aartsen et al. 2017) and  $E_\nu^2 F_\nu \sim (2 - 4) \times 10^{-10}$  GeV cm $^{-2}$ s $^{-1}$  in the energy range of  $E_\nu \sim 15$  TeV – 1 PeV expected for KM3NET with

six-year data (Aiello et al. 2019). The point source sensitivity in the figure is defined as the median upper limit at the 90% confidence level. We also compare  $F_\nu$  to the atmospheric muon and electron neutrino fluxes (Richard et al. 2016). A circular beam of  $1^\circ$  diameter is used for the fluxes in the figure.

With the adopted range of  $p_{\max} \simeq 1 - 100$  PeV/ $c$ , the  $\gamma$ -ray fluxes presented in the previous section are insensitive to  $p_{\max}$ , due to the exponential attenuation included in Equation (15). However,  $F_\nu(E_\nu)$  for high energy neutrinos exhibit strong dependence on the assumed value of  $p_{\max}$ . With larger  $p_{\max}$ ,  $F_\nu$  extends to higher energies. But the amount of highest energy neutrinos is determined not just by  $p_{\max}$ , but also by the diffusion model. If the diffusion timescale of CRPs is shorter at high energies,  $F_\nu$  should be lower. Hence,  $F_\nu$  is smaller at highest energies with the diffusion model B than with the diffusion model A in Figure 8. As mentioned in Section 3, in the diffusion model B, the streaming speed of CRPs approaches the speed of light at  $p \gtrsim 0.1$  PeV/ $c$ ; that is, the streaming speed may be overestimated and the diffusion timescale may be underestimated, and then  $F_\nu$  may be underestimated at highest energies. Yet, in all the models considered in Figure 8, which fit  $\gamma$ -ray observations reasonably well, the predicted  $F_\nu$  at  $E_\nu \gtrsim 0.1$  PeV from nearby SBGs is at least an order of magnitude smaller than the lower bound of the point source sensitivity of IceCube. Thus, SBGs may not be observed as point sources in IceCube. SBGs could be still a major contributor of diffuse high-energy neutrinos, as pointed in previous works (see the introduction for references), but the amount of estimated contributions should depend on the details of modeling including the diffusion model.

Our results suggest that nearby SBGs, especially M82 and also NGC253, might be resolvable as point sources in the range of  $10$  TeV  $\lesssim E_\nu \lesssim 1$  PeV with KM3NET in the most optimistic cases with the diffusion model A and  $p_{\max} = 100$  PeV/ $c$ , shown in Figure 8 (a) and (b). On the other hand, other models including those in Figure 8 (c) and (f) with the double PL model for SNR-produced CRPs and the diffusion model B, the combination that reproduces  $\gamma$ -ray observations best, predict  $F_\nu$  that does not touch the point source sensitivities box of KM3NET, indicating that nearby SBGs would be difficult to be detected as point sources. At lower energies of  $E_\nu \lesssim 1$  TeV, the neutrino flux has been obtained, for instance, in Super-Kamiokande (e.g., Hagiwara et al. 2019). However,  $F_\nu$  from nearby SBGs is predicted to be orders of magnitude smaller than the atmospheric muon neutrino flux. So it would not be easy to separate the signature of neutrinos from SBGs in the data of

ground facilities such as Super-Kamiokande and future Hyper-Kamiokande (e.g., Abe et al. 2011).

## 6. SUMMARY

We have estimated the CRP production by SWs from massive stars and SNRs from core-collapse SNe inside the SBN of nearby SBGs. Considering the lack of full understanding of nonlinear interrelationships among complex kinetic processes involved in the DSA theory, we have adopted both the canonical single PL model with  $\alpha_{\text{SN}}$  and the double PL model with  $\alpha_{\text{SN},1}$  and  $\alpha_{\text{SN},2}$  for the SNR-produced CRP momentum distribution. The latter is intended to represent a concave spectrum that might arise due to nonlinear dynamical feedback from the CR pressure, if  $\sim 10$  % of the shock kinetic energy is transferred to CRPs. For the SW-produced CRP distribution, only the single PL model with  $\alpha_{\text{SW}}$  is considered.

For the transport of CRPs inside the SBN, we have adopted two different diffusion models; CRPs scatter off either the large-scale turbulence of  $\delta B_{\text{SBN}}/B_{\text{SBN}} \sim 1$  present in the SBN (diffusion model A) or the waves self-excited by CR streaming instability (diffusion model B) (Peretti et al. 2019; Krumholz et al. 2020). The diffusion model B assumes that the pre-existing turbulence of scales less than the gyroradius of CRPs with  $E_{\text{CR}} \lesssim \text{several} \times 0.1$  PeV damps out by ion-neutral collisions.

Using the CRP momentum spectrum given in Equation (9) and the analytic approximations for source functions presented by Kelner et al. (2006), we have then calculated the  $\gamma$ -ray and neutrino emissions due to  $pp$  collisions in the SBN, and estimated their fluxes from three nearby SBGs, M82, NGC253, and Arp220, observable at the Earth.

Main findings are summarized as follows.

(1) If the single PL model for SNR-produced CRPs is adopted, the  $\gamma$ -ray observations of Fermi-LAT, Veritas, and H.E.S.S. can be reproduced only with the diffusion model A, but not with the diffusion model B. On the other hand, if the double PL model is adopted, the  $\gamma$ -ray observations can be reproduced with both diffusion models. The best results are obtained with the combination of the double PL model and the diffusion model B.

(2) The contribution of SW-produced CRPs may depend on the IGIMF; SBGs with higher SFRs are likely to flatter IGIMFs, resulting in larger ratios of  $\mathcal{L}_{\text{SW}}/\mathcal{L}_{\text{SN}}$ . In Arp220 where the star formation rate is high, the SW-produced CRPs may play an important role in the  $\gamma$ -ray emission.

(3) The predicted neutrino fluxes from three nearby SBGs seem too small, so that SBGs would not be observed as point sources in IceCube. On the other hand, our estimation suggests that M82 and NGC253 might be detectable as point sources in the upcoming KM3NeT, if the diffusion model A along with  $p_{\max} = 100$  PeV/c is employed. In other models, the predicted neutrino fluxes would not be high enough to be detected as point sources in KM3NeT.

Finally, Müller et al. (2020) recently suggested that high-energy processes associated with superwinds driven by the supersonic outflows from the SBN (not stellar winds) can produce CRPs as well. But their contribution to  $\gamma$ -ray emissions from SBGs would be  $\lesssim 10\%$ , so

that the main results of this paper would not be changed even when such contribution is included.

## ACKNOWLEDGMENTS

J.-H.H. and D.R. were supported by the National Research Foundation (NRF) of Korea through grants 2016R1A5A1013277 and 2017R1A2A1A05071429. J.-H. H. was also supported by the Global PhD Fellowship of the NRF through grant 2017H1A2A1042370. H.K. was supported by the Basic Science Research Program of the NRF through grant 2017R1D1A1A09000567.

## REFERENCES

- Aartsen, M. G., Abraham, K., Ackermann, M., et al. 2017, *ApJ*, 835, 151, doi: [10.3847/1538-4357/835/2/151](https://doi.org/10.3847/1538-4357/835/2/151)
- Abdo, A. A., Ackermann, M., Ajello, M., et al. 2010, *ApJL*, 709, L152, doi: [10.1088/2041-8205/709/2/L152](https://doi.org/10.1088/2041-8205/709/2/L152)
- Abdollahi, S., Acero, F., Ackermann, M., et al. 2020, *ApJS*, 247, 33, doi: [10.3847/1538-4365/ab6bcb](https://doi.org/10.3847/1538-4365/ab6bcb)
- Abe, K., Abe, T., Aihara, H., et al. 2011, arXiv e-prints, arXiv:1109.3262. <https://arxiv.org/abs/1109.3262>
- Acero, F., Aharonian, F., Akhperjanian, A. G., et al. 2009, *Science*, 326, 1080, doi: [10.1126/science.1178826](https://doi.org/10.1126/science.1178826)
- Acero, F., Ackermann, M., Ajello, M., et al. 2015, *ApJS*, 218, 23, doi: [10.1088/0067-0049/218/2/23](https://doi.org/10.1088/0067-0049/218/2/23)
- Aiello, S., Akrame, S. E., Ameli, F., et al. 2019, *Astroparticle Physics*, 111, 100, doi: [10.1016/j.astropartphys.2019.04.002](https://doi.org/10.1016/j.astropartphys.2019.04.002)
- Balogh, A., & Treumann, R. A. 2013, *Physics of Collisionless Shocks*, Vol. 12, doi: [10.1007/978-1-4614-6099-2](https://doi.org/10.1007/978-1-4614-6099-2)
- Bechtol, K., Ahlers, M., Di Mauro, M., Ajello, M., & Vandenbroucke, J. 2017, *ApJ*, 836, 47, doi: [10.3847/1538-4357/836/1/47](https://doi.org/10.3847/1538-4357/836/1/47)
- Bell, A. R. 1978, *MNRAS*, 182, 147, doi: [10.1093/mnras/182.2.147](https://doi.org/10.1093/mnras/182.2.147)
- Berezhko, E. G., & Ellison, D. C. 1999, *ApJ*, 526, 385, doi: [10.1086/307993](https://doi.org/10.1086/307993)
- Berezhko, E. G., & Völk, H. J. 2000, *A&A*, 357, 283, <https://arxiv.org/abs/astro-ph/0002411>
- Bykov, A. M. 2014, *A&A Rv*, 22, 77, doi: [10.1007/s00159-014-0077-8](https://doi.org/10.1007/s00159-014-0077-8)
- Bykov, A. M., Ellison, D. C., Osipov, S. M., & Vladimirov, A. E. 2014, *ApJ*, 789, 137, doi: [10.1088/0004-637X/789/2/137](https://doi.org/10.1088/0004-637X/789/2/137)
- Bykov, A. M., Marcowith, A., Amato, E., et al. 2020, *SSRv*, 216, 42, doi: [10.1007/s11214-020-00663-0](https://doi.org/10.1007/s11214-020-00663-0)
- Caprioli, D., Amato, E., & Blasi, P. 2010, *Astroparticle Physics*, 33, 160, doi: [10.1016/j.astropartphys.2010.01.002](https://doi.org/10.1016/j.astropartphys.2010.01.002)
- Caprioli, D., Blasi, P., Amato, E., & Vietri, M. 2009, *MNRAS*, 395, 895, doi: [10.1111/j.1365-2966.2009.14570.x](https://doi.org/10.1111/j.1365-2966.2009.14570.x)
- Caprioli, D., & Spitkovsky, A. 2014, *ApJ*, 783, 91, doi: [10.1088/0004-637X/783/2/91](https://doi.org/10.1088/0004-637X/783/2/91)
- Casse, M., & Paul, J. A. 1980, *ApJ*, 237, 236, doi: [10.1086/157863](https://doi.org/10.1086/157863)
- Cesarsky, C. J., & Montmerle, T. 1983, *SSRv*, 36, 173, doi: [10.1007/BF00167503](https://doi.org/10.1007/BF00167503)
- Drury, L. O. 1983, *Reports on Progress in Physics*, 46, 973, doi: [10.1088/0034-4885/46/8/002](https://doi.org/10.1088/0034-4885/46/8/002)
- Ekström, S., Georgy, C., Eggenberger, P., et al. 2012, *A&A*, 537, A146, doi: [10.1051/0004-6361/201117751](https://doi.org/10.1051/0004-6361/201117751)
- Freyer, T., Hensler, G., & Yorke, H. W. 2003, *ApJ*, 594, 888, doi: [10.1086/376937](https://doi.org/10.1086/376937)
- Georgy, C., Walder, R., Folini, D., et al. 2013, *A&A*, 559, A69, doi: [10.1051/0004-6361/201321226](https://doi.org/10.1051/0004-6361/201321226)
- H. E. S. S. Collaboration, Abdalla, H., Aharonian, F., et al. 2018, *A&A*, 617, A73, doi: [10.1051/0004-6361/201833202](https://doi.org/10.1051/0004-6361/201833202)
- Hagiwara, K., Abe, K., Bronner, C., et al. 2019, *ApJL*, 887, L6, doi: [10.3847/2041-8213/ab5863](https://doi.org/10.3847/2041-8213/ab5863)
- Janka, H.-T. 2012, *Annual Review of Nuclear and Particle Science*, 62, 407, doi: [10.1146/annurev-nucl-102711-094901](https://doi.org/10.1146/annurev-nucl-102711-094901)
- Kang, H. 2012, *Journal of Korean Astronomical Society*, 45, 127, doi: [10.5303/JKAS.2012.45.5.127](https://doi.org/10.5303/JKAS.2012.45.5.127)
- . 2013, *Journal of Korean Astronomical Society*, 46, 49, doi: [10.5303/JKAS.2013.46.1.049](https://doi.org/10.5303/JKAS.2013.46.1.049)
- Kang, H., & Jones, T. W. 2007, *Astroparticle Physics*, 28, 232, doi: [10.1016/j.astropartphys.2007.05.007](https://doi.org/10.1016/j.astropartphys.2007.05.007)
- Kang, H., & Ryu, D. 2010, *ApJ*, 721, 886, doi: [10.1088/0004-637X/721/1/886](https://doi.org/10.1088/0004-637X/721/1/886)
- . 2018, *ApJ*, 856, 33, doi: [10.3847/1538-4357/aab1f2](https://doi.org/10.3847/1538-4357/aab1f2)

- Kelner, S. R., Aharonian, F. A., & Bugayov, V. V. 2006, *PhRvD*, 74, 034018, doi: [10.1103/PhysRevD.74.034018](https://doi.org/10.1103/PhysRevD.74.034018)
- Kennicutt, R. C., & Evans, N. J. 2012, *ARA&A*, 50, 531, doi: [10.1146/annurev-astro-081811-125610](https://doi.org/10.1146/annurev-astro-081811-125610)
- Krumholz, M. R., Crocker, R. M., Xu, S., et al. 2020, *MNRAS*, 493, 2817, doi: [10.1093/mnras/staa493](https://doi.org/10.1093/mnras/staa493)
- Loeb, A., & Waxman, E. 2006, *JCAP*, 2006, 003, doi: [10.1088/1475-7516/2006/05/003](https://doi.org/10.1088/1475-7516/2006/05/003)
- Marcowith, A., Bret, A., Bykov, A., et al. 2016, *Reports on Progress in Physics*, 79, 046901, doi: [10.1088/0034-4885/79/4/046901](https://doi.org/10.1088/0034-4885/79/4/046901)
- Müller, A. L., Romero, G. E., & Roth, M. 2020, *MNRAS*, 496, 2474, doi: [10.1093/mnras/staa1720](https://doi.org/10.1093/mnras/staa1720)
- Murase, K., Ahlers, M., & Lacki, B. C. 2013, *PhRvD*, 88, 121301, doi: [10.1103/PhysRevD.88.121301](https://doi.org/10.1103/PhysRevD.88.121301)
- Palla, M., Calura, F., Matteucci, F., et al. 2020, *MNRAS*, 494, 2355, doi: [10.1093/mnras/staa848](https://doi.org/10.1093/mnras/staa848)
- Peng, F.-K., Wang, X.-Y., Liu, R.-Y., Tang, Q.-W., & Wang, J.-F. 2016, *ApJL*, 821, L20, doi: [10.3847/2041-8205/821/2/L20](https://doi.org/10.3847/2041-8205/821/2/L20)
- Peretti, E., Blasi, P., Aharonian, F., & Morlino, G. 2019, *MNRAS*, 487, 168, doi: [10.1093/mnras/stz1161](https://doi.org/10.1093/mnras/stz1161)
- Peretti, E., Blasi, P., Aharonian, F., Morlino, G., & Cristofari, P. 2020, *MNRAS*, 493, 5880, doi: [10.1093/mnras/staa698](https://doi.org/10.1093/mnras/staa698)
- Ptuskin, V. S., & Zirakashvili, V. N. 2005, *A&A*, 429, 755, doi: [10.1051/0004-6361:20041517](https://doi.org/10.1051/0004-6361:20041517)
- Richard, E., Okumura, K., Abe, K., et al. 2016, *PhRvD*, 94, 052001, doi: [10.1103/PhysRevD.94.052001](https://doi.org/10.1103/PhysRevD.94.052001)
- Romero, G. E., Müller, A. L., & Roth, M. 2018, *A&A*, 616, A57, doi: [10.1051/0004-6361/201832666](https://doi.org/10.1051/0004-6361/201832666)
- Seo, J., Kang, H., & Ryu, D. 2018, *Journal of Korean Astronomical Society*, 51, 37, doi: [10.5303/JKAS.2018.51.2.37](https://doi.org/10.5303/JKAS.2018.51.2.37)
- Sudoh, T., Totani, T., & Kawanaka, N. 2018, *PASJ*, 70, 49, doi: [10.1093/pasj/psy039](https://doi.org/10.1093/pasj/psy039)
- Tamborra, I., Ando, S., & Murase, K. 2014, *JCAP*, 2014, 043, doi: [10.1088/1475-7516/2014/09/043](https://doi.org/10.1088/1475-7516/2014/09/043)
- Tatischeff, V. 2009, *A&A*, 499, 191, doi: [10.1051/0004-6361/200811511](https://doi.org/10.1051/0004-6361/200811511)
- The VERITAS Collaboration, Abeysekara, A. U., Archambault, S., et al. 2015, arXiv e-prints, arXiv:1510.01639. <https://arxiv.org/abs/1510.01639>
- VERITAS Collaboration, Acciari, V. A., Aliu, E., et al. 2009, *Nature*, 462, 770, doi: [10.1038/nature08557](https://doi.org/10.1038/nature08557)
- Vladimirov, A. E., Bykov, A. M., & Ellison, D. C. 2008, *ApJ*, 688, 1084, doi: [10.1086/592240](https://doi.org/10.1086/592240)
- Wang, X., & Fields, B. D. 2018, *MNRAS*, 474, 4073, doi: [10.1093/mnras/stx2917](https://doi.org/10.1093/mnras/stx2917)
- Weaver, R., McCray, R., Castor, J., Shapiro, P., & Moore, R. 1977, *ApJ*, 218, 377, doi: [10.1086/155692](https://doi.org/10.1086/155692)
- Zirakashvili, V. N., & Ptuskin, V. S. 2012, *Astroparticle Physics*, 39, 12, doi: [10.1016/j.astropartphys.2011.09.003](https://doi.org/10.1016/j.astropartphys.2011.09.003)
- . 2016, *Astroparticle Physics*, 78, 28, doi: [10.1016/j.astropartphys.2016.02.004](https://doi.org/10.1016/j.astropartphys.2016.02.004)
- . 2018, *Astroparticle Physics*, 98, 21, doi: [10.1016/j.astropartphys.2018.01.005](https://doi.org/10.1016/j.astropartphys.2018.01.005)